Modelling and Analysis of Wirelessly Interrogated SAW based Micropumps for Drug Delivery Applications

by

Don Wenura Eranda Dissanayake

B. Eng Computer Systems (First Class Honours),
University of Adelaide, 2004

Thesis submitted for the degree of

Doctor of Philosophy

in

School of Electrical and Electronic Engineering,
Faculty of Engineering, Computer and Mathematical Sciences
The University of Adelaide

April 2010

Chapter 4

Corrugated Microdiaphragm Design

THIS chapter presents modelling and analysis of a microdiaphragm that is designed for the implantable micropump. Microdiaphragms are considered to be a major component of micropumps. However, for low–powered MEMS applications, displacement enhancement methods need to be addressed. Therefore, various methods for displacement enhancement are discussed and Finite Element Modelling (FEM) and Analysis (FEA) were carried out to model the microdiaphragm. Furthermore, as an extension of the analysis presented in Chapter 3, the Rayleigh–Ritz method based analytical model was developed mainly to validate the results obtained through FEA. During FEA, a 3D model of the diaphragm is developed and various types of corrugation profiles were considered to enhance the device performance. A coupled–field analysis was carried out to model the electrostatic–solid interaction between the corrugated microdiaphragm and the SAW device. Static and transient analysis methods were implemented in microdiaphragm analysis.

Moreover, the performance of corrugated microdiaphragms were extensively evaluated in this Chapter, and the relationship between different corrugation types, corrugation parameters, and stress distribution is also presented. Additionally, a basic device structure is fabricated and tested, and developments for improvements are also discussed.

4.1 Introduction

The functionality of the microdiaphragm in a wirelessly actuated micropump plays a major role in low–powered device actuation. In developing micropumps and their components, it is becoming an increasing trend to predict the performance before the prototype is fabricated. Because performance prediction allows for an accurate estimation of yield and lifetime, in addition to developing better understanding of the device while taking into account the details of the device structure and second order effects. Hence avoid potential pitfalls in the device operation in a practical environment.

Various approaches have been pursued in the process of design, development and realisation of these micropumps, microfluidic operation and its peripherals, such as microdiaphragms and diffuser elements. Simulation of diaphragm–based, valveless micropumps using FEA tools has become more popular, due to the availability of advanced simulation tools and computational power (Nisar *et al.* 2008c, Tsui and Lu 2008, Cui *et al.* 2008). Alternatively, analytical models have also been used for the analysis of diaphragm based actuation mechanisms (Lee and Kim 2000, Olsson *et al.* 2000, Français 2000). Both of these methods facilitate the design of a model with optimal operating conditions prior to device fabrication.

The optimisation and verification of individual components of a micropump to achieve the desired performance of an integrated system is highly important. Therefore, in this chapter, the design and analysis of low–powered, electrostatically controlled corrugated microdiaphragms is carried out using both FEA and analytical modelling techniques. As was introduced in previous chapters, in this research, a novel, fully passive, wireless and secure interrogation methodology based actuation mechanism is used, to operate the microdiaphragm; hence the micropump for drug delivery and related biomedical applications.

Organisation of this chapter is as follows. Section 4.2 briefly summarise the operation of the micropump structure, and the SAW device based secure actuation mechanism. More details on the SAW device based secure actuation is presented in Chapters 2 and 3. The design of microdiaphragm structures is presented in Section 4.3, and in Section 4.4 Rayleigh–Ritz method based analytical model is presented and discussed. Then in Section 4.5, more emphasis is given towards FEM using ANSYS simulations tools (ANSYS Incorporation 2009b). The results achieved through FEA are presented and discussed in Section 4.6. Section 4.7 presents the initial fabrication process

of the microdiaphragm. Consequently, Section 4.8 highlights challenges and expected future work and is followed by a conclusion in Section 4.9.

4.2 SAW Device based Microdiaphragm Actuation

As discussed in Chapters 2 and 3, SAW devices are widely used in MEMS applications, which require secure, wireless, and passive interrogation (Jones *et al.* 2008). Here the implementation of this unique approach for the wireless actuation of a microdiaphragm is investigated. As shown in Figure 4.1, the micropump is mounted on top of the SAW device, such that the microdiaphragm is directly placed on top of the output IDT. As a result the microdiaphragm can be actuated wirlessly similar to the method introduced in earlier chapters.

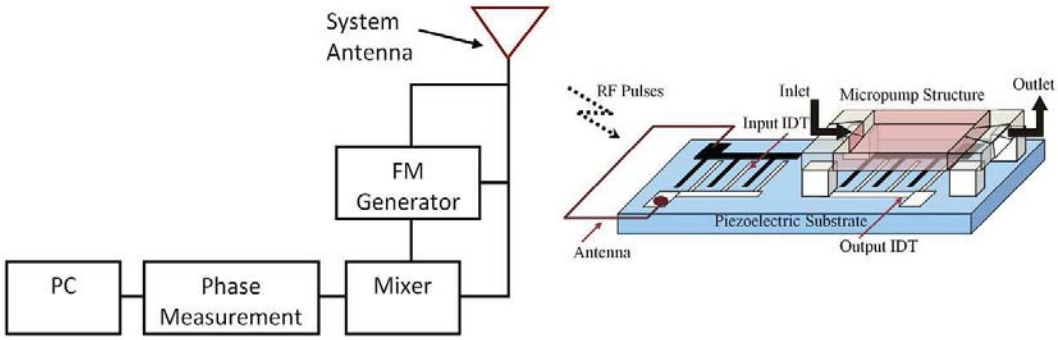

Figure 4.1. Wireless interrogation unit for SAW device based micropump. SAW device consist of a piezoelectric substrate, input IDT, and output IDT. Input IDT is connected to a micro-antenna for wireless communication. The micropump structure is placed on top of the output IDT of a coded SAW device, which securely controls the microdiaphragm.

4.2.1 Micropump Operating Principle

As can be seen from Figure 4.1, the interrogation approach adopted in this thesis is based on conventional Radio Frequency Identification Device (RFID) technology where low power circuits can obtain their power from an electromagnetic field. Additionally, the implantable device is designed to achieve this by not having any active electronic circuitry. Figure 4.1 shows a setup for interrogating a SAW device with an integrated antenna. The valveless micropump structure is mounted on top of the output IDT of the SAW device (SAW correlator). This micropump structure consists of a

thin conductive microdiaphragm, a fluid chamber, and inlet and outlet diffusers. As shown in Figure 4.2, the gap between the conductive diaphragm and the output IDT is set to be a few micrometers.

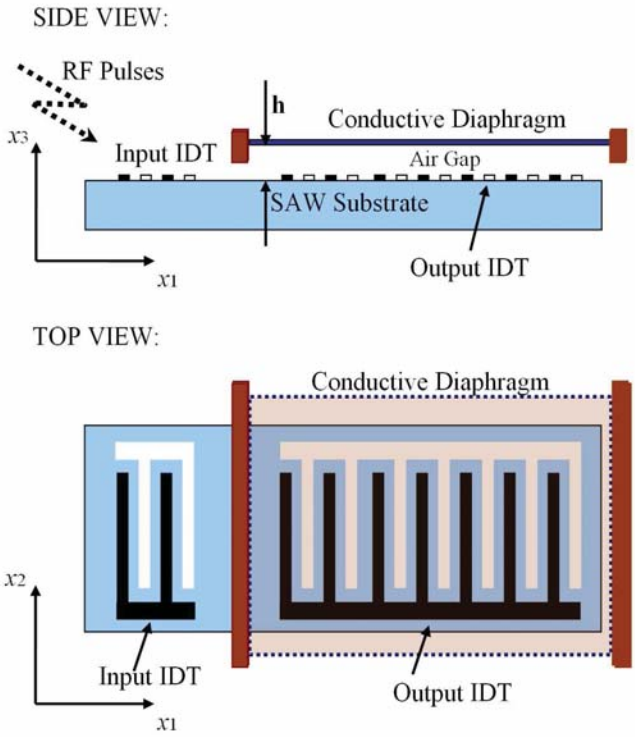

Figure 4.2. Positioning of the microdiaphragm on SAW device. Side view: Air-gap separated diaphragm is placed above the output IDT of the SAW device. Top view: The area of the diaphragm is larger than the effective area of the output IDT, hence allows more deflection as the stress levels at the central area of the diaphragm is less.

Here, the SAW device receives a coded RF signal power, which is directly converted to stress waves in the piezoelectric substrate, using the converse piezoelectric effect. These mechanical stress waves propagate along the planar surface of the piezoelectric substrate and then reconverted to an electric signal at the output IDT due to the piezoelectric effect. However, as explained in previous chapters, only when the code in the interrogating RF signal matches the embedded code in the output IDT, a signal with high amplitude (high processing gain) is generated at the output IDT (Tikka *et al.* 2007). Consequently, an electrostatic field is generated between the output IDT and the conductive diaphragm, and the resulting electrostatic force cause a deflection in the microdiaphragm. This deflection in the microdiaphragm, along with carefully designed diffusers are used to cause the required microfluidic flow manipulations.

4.3 Corrugated Microdiaphragm Modelling

A diaphragm is essentially a thin circular or rectangular plate, made out of a flexible material, stretched and fastened at its periphery. Diaphragms are widely used as sensing elements in MEMS devices, for high accuracy and good dynamic response. Periphery–clamped flat diaphragm having high residual stress in the film may give rise to undesirable effects such as much higher actuation voltage, film buckling, or even membrane cracking. Generally the main characteristics of a diaphragm are ruggedness, excellent stability and reliability, low hysteresis and creep, and good dynamic response. Moreover, other characteristics such as effect of the environmental conditions, material of the diaphragm, size, weight, and fabrication technology vary significantly, depending on the transduction principle in use, range, and actual application (Rangan *et al.* 1983, Soin and Majlis 2006).

The main considerations when selecting a suitable diaphragm material for drug delivery applications are the chemical nature of the fluid/drug that is expected to come in contact with the diaphragm, temperature range, effects of shock and vibration, and frequency response requirements (Rangan *et al.* 1983). Performance of the diaphragm can be improved when it is cycled a number of times over the expected range of operating temperatures. It is important to incorporate the pressure cycling and heat treatment, at the manufacturing stage, to reduce the *elastic-after effects* of the diaphragm. In this way, the consistency and the reproducibility of the diaphragm operation can be increased (Rangan *et al.* 1983, Soin and Majlis 2006). Moreover the mechanical sensitivity of the diaphragm can be improved by both releasing the initial stress and reducing the bending stiffness of the diaphragm (Wang *et al.* 2003).

4.3.1 Displacement Enhancement Methods

For most thin diaphragms, a large tensile stress can lead to undesirable effects such as low and irreproducible performances, if the processes cannot accurately be controlled. As a result, the displacement characteristics can be affected as well. In order to design diaphragms with low–stress and higher displacements, various design techniques can be followed (Ke *et al.* 2009, Wang *et al.* 2003, Giovanni 1982). One such technique is to use a sandwich structure in which layers with compressive and tensile stress are combined. Another stress releasing technique is to form corrugations in the diaphragm, which is considered to be an effective way to alleviate the residual stress

in diaphragm (Ke *et al.* 2009). Corrugated diaphragms have been verified to be capable of releasing the built–in stress, thereby increasing the mechanical sensitivity of the diaphragm and reducing the irreproducibility (Wang *et al.* 2003). This results in requiring a low actuation voltage to drive microdiaphrgm based structures.

Compared with conventional flat diaphragms, the shallowly corrugated diaphragms have demonstrated improved sensitivity, especially for a high residual stress level (Soin and Majlis 2006, Giovanni 1982). Although shallow corrugation technique can sufficiently reduce the membrane rigidity of the diaphragm, the bending rigidity, however, may be largely increased due to the increased '*equivalent thickness*' of the diaphragm (Wang *et al.* 2003). The effect of the corrugated profiles in achieving higher displacements is further discussed and analysed in the following subsection.

4.3.2 Corrugated Diaphragm Design

The structure of the diaphragm may be flat or corrugated depending on the intended MEMS application. Flat diaphragms are used for most of the sensing related applications. However for applications where large displacements are desired, corrugated diaphragm structures are ideally suited (Rangan *et al.* 1983). Corrugated diaphragms are made by forming concentric beads or corrugations on a thin sheet of metal (or a similar material). As a result, such diaphragms increase in rigidity and become suitable for operation at larger displacements, and longer linear travel than flat diaphragms (Giovanni 1982). As it can be seen from the Figure 4.3, various types of corrugation profiles such as sinusoidal, toroidal, sawtooth, and trapezoidal are being used for MEMS applications (Ke *et al.* 2009, Giovanni 1982, Wang *et al.* 2009).

These diaphragms can be operated either as a single element or for higher sensitivity as a capsule, having two diaphragms facing one another, and such structures can be used in designing actuators for micropumps, since higher displacements are achievable from the capsule like designs. It has been suggested that the shape of the profile has little effect on the performance characteristics of the diaphragm (Giovanni 1982). In general, diaphragms with fine sawtooth profiles are simple to manufacture and are stable at small overloads. However, manufacturing of diaphragms with deep sawtooth profiles is comparatively difficult due to the possibility of cracks developing at crests due to stress concentration. Whereas, the fabrication of diaphragms having sinusoidal and similar shaped corrugations needs more complex tools (Giovanni 1982). But in

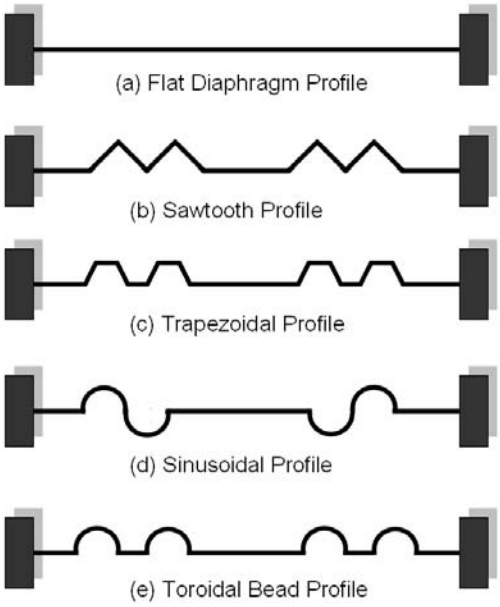

Figure 4.3. Different types of corrugated profiles.. The selection of a certain corrugation profile depends on the specific application and the fabrication ease.

such corrugation profiles, the stress concentration is minimal compared to sawtooth and trapezoidal profiles. However, due to the minimal stress concentration feature, sinusoidal and toroidal profiles are found to be attractive, and performance analysis for such profiles are conducted in this chapter and presented in Section 4.6. In analysing such corrugated diaphragms, the focus is directed towards the variation in corrugation parameters.

4.3.3 Corrugation Parameters

Corrugation wavelength (L), corrugation height (H), corrugation thickness (t_D), and number of corrugation wavelengths (N) are considered to be the critical parameters in designing sinusoidal and toroidal corrugations as depicted in Figure 4.4. The ratios H/t_D, and L/H need to be carefully considered to reduce the unnecessary stress concentrations around the corrugations (Giovanni 1982).

Different methods are mentioned in literature for the design of sinusoidal corrugations (Giovanni 1982, Wang *et al.* 2009). Especially in analytical approaches, tangent arcs have been used to develop approximated sinusoidal shapes (Lee and Kim 2000). Therefore, in order to compare the effectiveness in each method, sinusoidal corrugations were designed in two different methods, (i) the approximation of sinusoidal

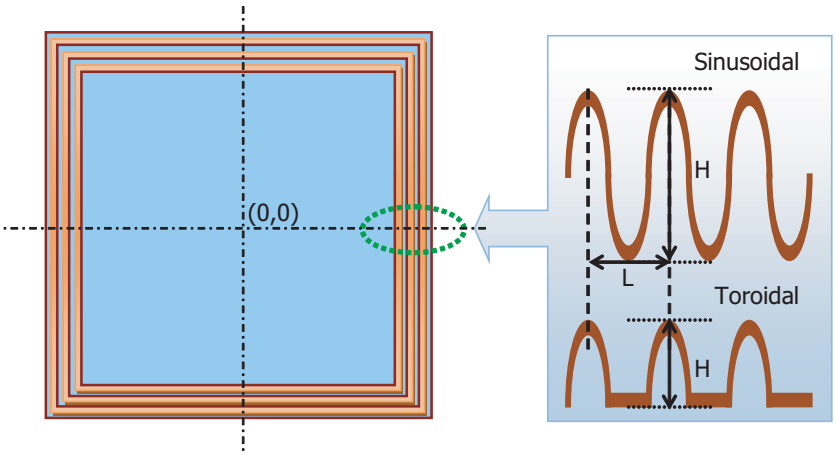

Figure 4.4. Corrugation profiles and parameters for a rectangular diaphragm. Sinusoidal and Toroidal corrugation profiles and associated corrugation parameters. Here, L denotes the corrugation wavelength and H is the corrugation height. A square diaphragm is considered for the analysis, as it is easier to fabricate and mount such a diaphragm on a SAW device, compared to a circular diaphragm.

shape with tangent arcs, and (ii) the use of pure–sinusoidal shaped corrugations. Then, analysis is conducted to evaluate the performance of diaphragms with these types of sinusoidal corrugations, along with the toroidal shaped corrugations, and results are discussed in Section 4.6.

4.4 Analytical Model for Microdiaphragm Actuation

4.4.1 Electrostatic Force Generation

In Chapter 3, a theory was developed and presented for the SAW device based electrostatic actuation principle. In this section, this theory is extended for the SAW device based microdiaphragm actuation principle. In electrostatic actuation, the electrostatic attraction force F applied on two parallel conductive plates (electrodes) can be described using the parallel plate capacitor effect (Tsai and Sue 2007) as

$$F = \frac{1}{2}\frac{\varepsilon A \Phi^2}{(h - W_D)^2}, \tag{4.1}$$

where ε is the dielectric coefficient of the medium between the plates, A is the effective plate area, W_D is the instantaneous deflection of the microdiaphragm in x_3 direction, h is the initial plate spacing, and Φ is the applied electric potential between the plates.

Based on the analysis presented in Chapter 3, the electric potential at the output IDT region can found to be a combination of both the electric potential at the IDT fingers, and the electric potential at the IDT finger gaps, as shown by Equation 4.2.

$$\Phi(x_1,x_3,t)=\begin{cases}\Psi, & for \quad n\lambda \le x_1 \le (\frac{1}{4}+n)\lambda \\ \Omega, & for \quad (\frac{1}{4}+n)\lambda < x_1 < (\frac{1}{2}+n)\lambda \\ -\Psi, & for \quad (\frac{1}{2}+n)\lambda \le x_1 \le (\frac{3}{4}+n)\lambda \\ -\Omega, & for \quad (\frac{3}{4}+n)\lambda < x_1 < (1+n)\lambda \end{cases}, \tag{4.2}$$

$$\text{where } \Psi=\frac{2T}{\pi^2}\Phi(\frac{\lambda}{8},x_3,t),\ \Omega=\Phi(x_1,x_3,t), \text{ and } n=0,1,2,...,(N_p-1),$$

$$\text{for } \Phi(x_1,x_3,t)=\left[\sum_m C_m\alpha_4^m e^{ikb^m x_3}\right]e^{ik(x_1-vt)}, \text{ and } m = 1,\ 2,\ 3,\ 4.$$

Here N_p is the total number of finger pairs in the output IDT, and λ is the SAW wavelength. C_m values are the weighting coefficients of these electric potential equations and are defined based on the mechanical and electrical boundary conditions of the system. α_4^m (for $m = 1,\ 2,\ 3,\ 4$) are linear coefficients that are dependent on the decaying constant b. v is the SAW velocity in the piezoelectric substrate in the x_1 direction, k is the wave number, and $T\ (=\lambda/v)$ is the time period of the SAW. The coordinate system used in these equations is defined in Figure 4.2 and the IDT geometry for one wavelength (one period) of the SAW is shown in Figure 4.5.

As was elaborated in Chapter 3, as well as explained in Section 4.2.1, an electrostatic force is generated between the output IDT and the conductive diaphragm, due to the time varying electric potential at the output IDT. As was presented in Chapter 3, to formulate this force, each finger gap is divided into N_s subdivisions in the x_1 direction, so that each subdivision has a width of $\frac{f_w}{N_s}$ and a length of f_l ($\approx$ aperture of the IDT). Combining Equations 4.1 and 4.2, and after some algebraic simplifications, the total resultant electrostatic force can be evaluated as

$$F_{(Tot)}=\frac{C}{(h-W_D)^2}\sum_j\left[\left(\frac{2T}{\pi^2}\right)^2\Phi^2(\frac{\lambda}{8},x_3,t)+\Phi^2(\frac{\lambda}{4}+\frac{j\lambda}{4N_s},x_3,t)\right], \tag{4.3}$$

for j = 1, 2, 3,.., N_s and $C=\frac{\varepsilon_0 f_l f_w N_p}{N_s}$.

While the diaphragm is stretched due to the applied electrostatic force, an elastic restoring force is developed in the diaphragm. At equilibrium, the diaphragm's kinetic

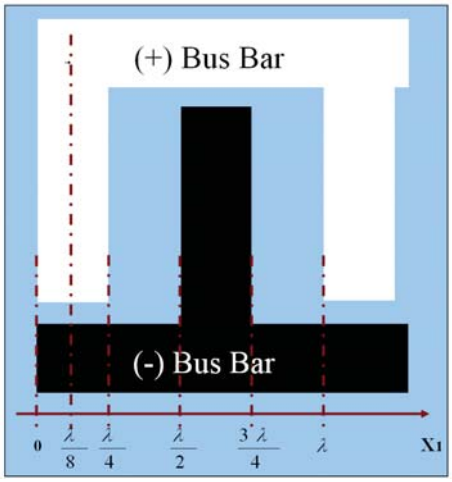

Figure 4.5. Periodic IDT finger representation. IDT finger representation for one wavelength (λ) with a metalisation ratio of $\frac{1}{2}$. Each finger is connected to one of the two bus bars, with one bus bar assigned a positive value and the other assigned a negative value.

energy becomes zero. Therefore, to determine the displacement achieved by the diaphragm, the calculated electrostatic force and the elastic restoring force need to be considered at their equilibrium point (Gilbert *et al.* 1996, Hu *et al.* 2004). However, this electrostatic–solid interaction scenario become a complex problem to solve since both forces depend on the instantaneous diaphragm displacement $W_D(x_1, x_2)$. Therefore, to obtain an accurate solution for $W_D(x_1, x_2)$, both analytical methods and numerical analysis methods are exploited in this research to analyse the corrugated diaphragm performance. The analytical model discussed here is used to validate the results obtained from FEA simulations.

4.4.2 Rayleigh–Ritz Method for Diaphragms

This is an extended version of the analysis presented in Chapter 3, which was developed to analyse the performance of a SAW device based electrostatic actuator using Rayleigh-Ritz method. Here, an energy minimisation technique is used to solve the problem for corrugated diaphragm model.

For a rectangular microdiaphragm with a length of $2a$ and a width of $2b$, the total energy E_{dia} of the diaphragm under pressure P can be written as (Bao 2000);

$$\begin{aligned} E_{dia} &= E_1 - E_2 - E_3, \\ E_1 &= \int_{-b}^{b}\int_{-a}^{a} \frac{\mathbb{D}}{2}\left(\frac{\partial^2 W_D}{\partial x_1^2} + \frac{\partial^2 W_D}{\partial x_2^2}\right)^2 dx_1 dx_2, \\ E_2 &= \int_{-b}^{b}\int_{-a}^{a} \mathbb{D}(1-\nu)\left[\frac{\partial^2 W_D}{\partial x_1^2}\frac{\partial^2 W_D}{\partial x_2^2} - \left(\frac{\partial^2 W_D}{\partial x_1 \partial x_2}\right)^2\right] dx_1 dx_2, \\ E_3 &= \int_{-b}^{b}\int_{-a}^{a} P W_D dx_1 dx_2, \end{aligned} \tag{4.4}$$

where $D = \frac{\mathbb{E}{t_D}^3}{12(1-\nu^2)}$ is the bending stiffness, $\mathbb{E}$ is the modulus of elasticity, t_D is the diaphragm thickness and ν is the Poisson ratio of the diaphragm material. Considering the relation $F = P.A$, where A is the effective diaphragm area, the term E_3 in Equation 4.4 can be rearranged using the electrostatic force derived in Equation 4.3. In Equation 4.4, the displacement function $W_D(x_1, x_2)$ must satisfy the essential homogeneous boundary conditions of the microdiaphragm, which take the following form.

$$\begin{aligned} W_D(\pm a, x_2) &= W_D(x_1, \pm b) = 0, \\ \frac{\partial W_D}{\partial t}\,|_{x_1=\pm a} &= \frac{\partial W_D}{\partial t}\,|_{x_2=\pm b} = 0. \end{aligned} \tag{4.5}$$

Now, based on the essential boundary conditions of the model, a displacement function for the rectangular diaphragm is considered as

$$W_D(x_1, x_2) = K_D(a^2 - {x_1}^2)^2(b^2 - {x_2}^2)^2, \tag{4.6}$$

with the only unknown being the constant K_D. Here, $(x_1, x_2) \equiv (0, 0)$ denotes the center of the diaphragm in x_1x_2 plane as depicted in Figure 4.4. Constant K_D can be evaluated by substituting Equations 4.3 and 4.6 into Equation 4.4, and by minimising the total energy E_{dia} with respect to K_D by calculating the derivative as in Equation below.

$$\frac{\partial E_{dia}}{\partial K_D} = 0. \tag{4.7}$$

The convergence is achieved by following an iterative approach, due to the complicated nonlinear coupling between Equations 4.3–4.6.

In order to utilise this analytical model to analyse the performance of corrugated microdiaphragm, hence to validate FEA simulations, equivalent bending stiffness method

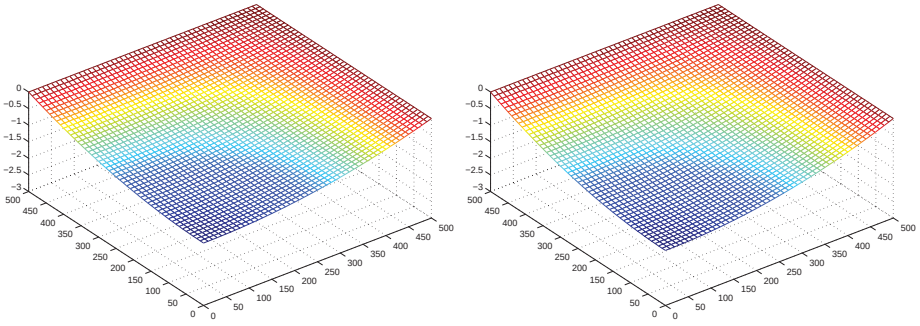

(a) $V_{in} = 1V$ (b) $V_{in} = 2V$

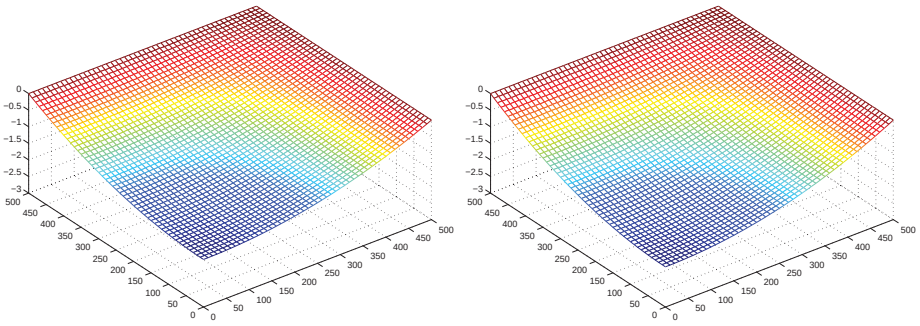

(c) $V_{in} = 4V$ (d) $V_{in} = 6V$

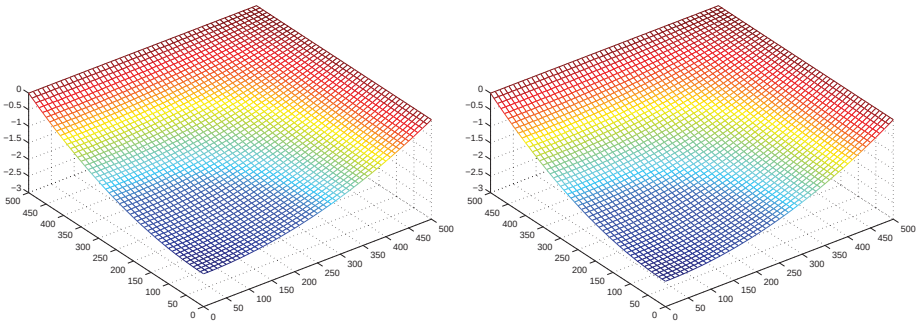

(e) $V_{in} = 8V$ (f) $V_{in} = 10V$

Figure 4.6. Diaphragm deflection performance. Mid–node deflection ($W_D(0,0)$) of the diaphragm for different input voltages (V_{in}). As the control voltage increases, $W_D(0,0)$ increases at an increasing rate. The dimensions of diaphragms presented in this figure are 1000 μm $\times$ 1000 μm (Length $\times$ Width).

(Lee and Kim 2000) and residual stress reduction method (Ke *et al.* 2009, Füldner *et al.* 2005) are used for sinusoidal and toroidal profiles, respectively. However, to reduce

the complexity of the model, these methods are associated with assumptions and simplifications such as exclude both the Poisson effect for corrugated part, and the bending stiffness in tangential direction for highly stressed and shadow corrugations. Diaphragm deformations for various operating voltages are achieved and presented in Figure 4.6 . As can be seen from this figure, a higher actuation voltage results in higher mid–node displacements.

As was discussed previously, analytical approaches with reduced simplifications are quite complicated and requires extensive computational effort. In solving such problems, numerical methods such as Finite Element Analysis (FEA) have been commonly used in relation to MEMS applications (Bao 2000, Nisar *et al.* 2008b). Because of the complexity in analysis, which involves electrostatic and structural field couplings in a complicated geometry due to the corrugations, FEA of the corrugated microdiaphragm is developed using ANSYS simulation tools and presented in Section 4.5.

4.5 ANSYS based Finite Element Modelling

As discussed previously in Chapter 3, a coupled–filed analysis is required to model the electrostatic–solid interaction, during Finite Element Analysis (FEA) of the microdiaphragm. Generally, direct-coupling is advantageous for coupled-field interactions which involves strongly coupled physics or high nonlinearity which is best solved in a single solution. However, analysis based on load transfer methods are more efficient and flexible because the different field analysis could be performed independently. Load transfer method based ANSYS Multi–field solver (MFX) is available for a large class of coupled analysis problems, and more suitable for MEMS based coupled–field analysis which involves interaction between multiple physics fields (Nisar *et al.* 2008c). Therefore in this research, ANSYS–MFX solver is used to analyse the microdiaphragm performance.

4.5.1 Preparation of the Model for the Analysis

The accuracy of FEA depends on factors such as node density of the mesh, appropriate element type, and accurate application of boundary conditions. Additionally, these factors form a tradeoff between accuracy and simulation time. Therefore, extra care is needed in meshing the geometry, especially when analysing the effect of the

corrugation parameters on the diaphragm displacement. The geometry of the microdiaphragm is meshed carefully considering factors such as element types and their capabilities, and element sizes, to avoid any unwanted distortion in elements hence to obtain accurate results.

Here, SOLID95 element type was used for the structural model including 3D corrugations, since it can tolerate irregular shapes without much loss of accuracy compared to the other solid elements in ANSYS (ANSYS Incorporation 2009b). Additionally, as was discussed in Chapter 3, SOLID95 elements are well suited to model curved boundaries, and has capabilities such as plasticity, creep, stress stiffening, large deflection, and large strain capability hence highly suitable for the design of corrugations (Lakshminarayana 2004). Electrostatic air–gap beneath the diaphragm was meshed using SOLID122 element type. This element type was used because it has compatible voltage shapes that are applicable to 3D electrostatic and time–harmonic electric field analysis (ANSYS Incorporation 2009b). Geometries of SOLID95 and SOLID122 are shown in Figure 4.7.

NOTE:
This figure is included on page 98
of the print copy of the thesis held in
the University of Adelaide Library.

Figure 4.7. SOLID95 and SOLID122 element geometries. 3D, 20–node elements used in designing the microdiaphragm with corrugations, and the air–gap between the electrodes. Even though both SOLID95 and SOLID122 have the same geometrical shape, they are designed to model different material and/or different physical properties (ANSYS Incorporation 2009a). SOLID95 element has capabilities such as plasticity, creep, stress stiffening, large deflection, and large strain capability. SOLID122 is a charge based electric element with one DoF (Voltage) at each node. SOLID122 elements are well suited to model curved boundaries and applicable to 3D electrostatic and time–harmonic quasi–static electric field analysis (ANSYS Incorporation 2009a).

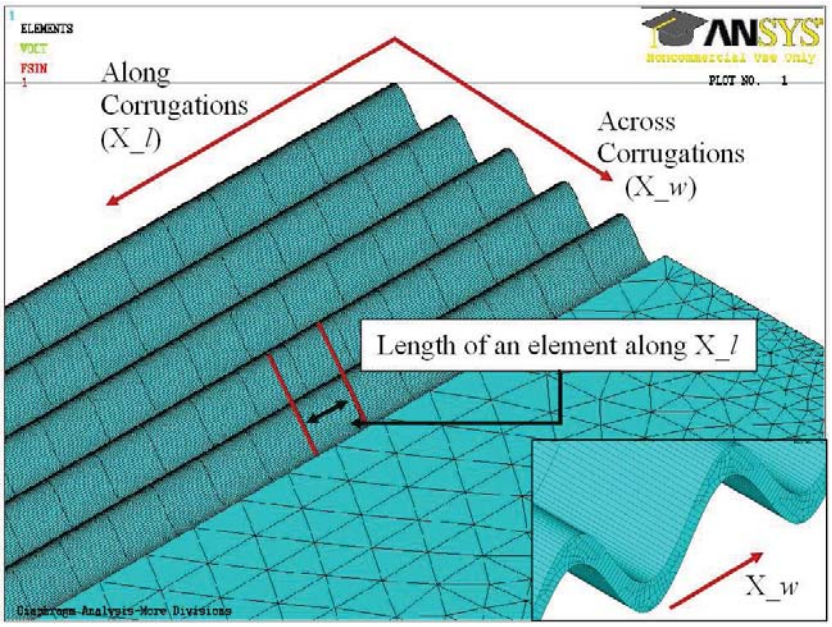

Figure 4.8. View of the corrugations in meshed diaphragm model. Here X_l denotes the direction along the corrugations and X_w denotes the direction across the corrugations towards the mid section.

4.5.2 Effective Mesh Generation

In electrostatic–solid coupling, forces get transferred from the electrostatic field to the solid diaphragm and displacements get transferred from the solid to the electrostatic field, which requires a suitable mesh density at the interface.

In the proposed microdiaphragm model, the effect of the output IDT is incorporated by coupling a set of nodes at the bottom of the air–gap to match the desired IDT pattern, and assigning the Volt DoF to those nodes. It should be noted that the width of each IDT finger (and finger gaps) is designed to be 10 μm ($= \lambda/4$ for an operating SAW frequency of 50 MHz and SAW velocity of 4000 m/s). Therefore, for an accurate representation of the output IDT, smaller element size is need at the air–gap model as well. In total, approximately 300,000–350,000 nodes are used for these simulations to accomplish the expected accuracy. With the availability of systems with high processing power, such simulations have become more practical nowadays than in the past.

During the initial analysis, simulations were carried out with differently meshed models until the results are converged. This is to highlight the fact that accurate results not only just depend on the node density alone, but also on how well the critical sections

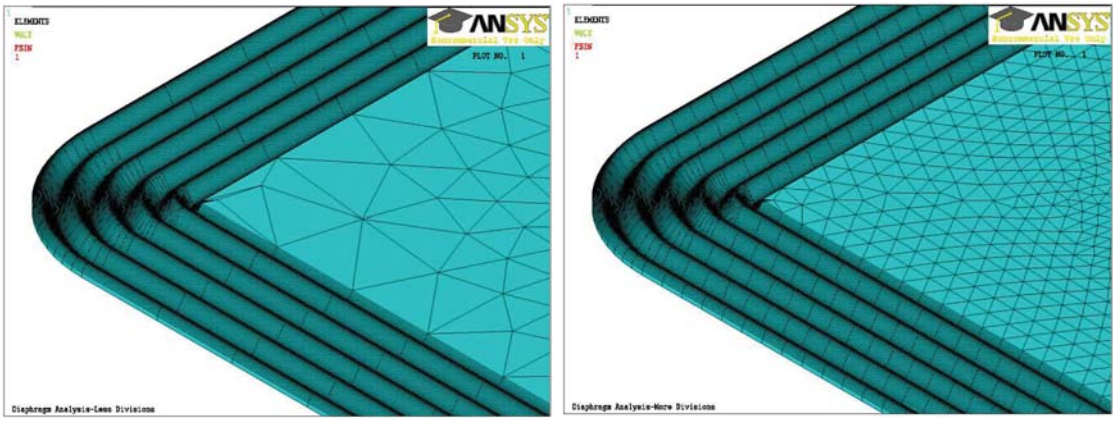

(a) Meshed corrugations with 25 divisions per side along X_l

(b) Meshed corrugations with 75 divisions per side along X_l

Figure 4.9. Various mesh densities. (a) results in a coarse mesh and (b) a finer mesh. Mesh density in corrugated section affects the mesh density in adjacent flat section.

are meshed considering the physics associated with the model. Figure 4.8 explains the different directions considered in each approach to vary the node density in corrugated and flat sections.

In the first approach, the node density is changed along X_l direction by varying the length of elements. However, this in turn cause an effect on node density of the flat section of the diaphragm as can be seen from Figure 4.9. In the second approach, the node density is varied along X_w direction. Once the resolution in corrugated section is established, the element size in the flat section is varied to decide upon an appropriate mesh density for flat section, to represent the output IDT accurately. The way these changes affect the accuracy is further discussed in Section 4.5.3.

4.5.3 Effect of Mesh Density on Accuracy

In this section, the analysis is further expanded by considering the same geometric model but with different mesh configurations by utilising different mesh parameters, that affect the total number of nodes used for the mesh. Three kinds of mesh variations are considered in initial simulations and the convergence results are presented in Figures 4.10 and 4.11.

In Figure 4.10, the percentage variation is the variation in the mid–node displacement of the diaphragm from one simulation to the next simulation, as the total number of nodes are increased. In general, results converge (percentage variation decreases up to 1%) as the total number of nodes used for the model increases. However, there is not much variation in the results as the node density is changed along X_l. This is because bending stiffness in corrugations along X_l direction is negligible, hence does not contribute much towards the sensitivity (Füldner *et al.* 2005), and additional nodes along that direction does make little difference.

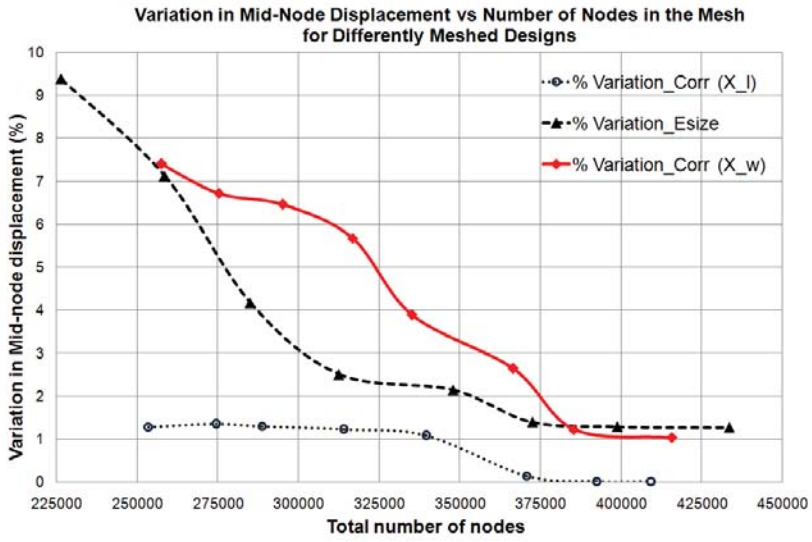

Figure 4.10. Percentage Variation in Mid–node Displacement (PVMD). PVMD of the diaphragm VS total number of nodes. Three scenarios are considered. % Variation_Corr (X_l) : PVMD as the node density is varied along X_l direction. % Variation_Esize : PVMD as the element size is varied for flat section. % Variation_Corr (X_w) : PVMD as the node density is varied along X_w direction. X_l and X_w are defined in Figure 4.8.

In contrast, higher variations are observed when the node density is changed along X_w direction. It is known that the tensile rigidity in the radial direction is smaller in a corrugated diaphragm and has a dominant effect towards the overall sensitivity (Giovanni 1982). Additionally, when the diaphragm is deflected due to the applied electrostatic force, an elastic restring force is generated in the diaphragm that is directed towards the diaphragm center. As a result, a higher node density in X_w direction allows for a better representation of the corrugations and produce more accurate results. Figure 4.11 depicts the simulated displacement variation with total number of

nodes. In any of the three scenarios, it is evident that the displacement approached approximately 3 μm as the number of nodes increased.

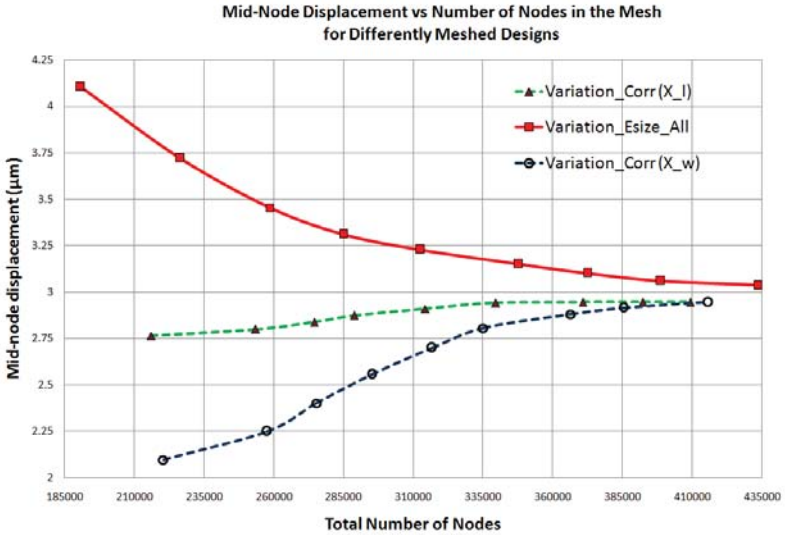

Figure 4.11. Mid–node Displacement (MnD) of the diaphragm VS total number of nodes. Three scenarios are considered. Variation_Corr (X_l) : MnD as the node density is varied along X_l direction. Variation_Esize : MnD as the element size is varied for flat section. Variation_Corr (X_w) : MnD as the node density is varied along X_w direction. X_l and X_w are defined in Figure 4.8.

Similarly, smaller element sizes in flat section (including the air–gap) has a substantial effect on overall accuracy. As can be seen in Fig. 4.12, smaller elements allows for a good representation of the output IDT structure by clearly defining positive and negative electrode fingers. As a result during simulations, increased accuracy was observed in the interpolated force and displacement values, at the fluid–structure interface. Therefore as the element size decreases from 15 μm to 3 μm over a few simulations, a convergence was noticed. However, an element size of 5 μm was selected for the rest of the simulations as it produced result within only 1% variation. Once the overall convergence was achieved, as presented in Section 4.6.1, further analysis was carried out to compare diaphragms with different corrugations types.

4.5.4 Material Selection

As was mentioned before, the micropump device is targeted at biomedical applications. Therefore a careful selection of biocompatible materials is of high regard. The

Figure 4.12. Representation of output IDT with different meshes. (a) Output IDT is properly represented in a finely meshed model with an element size of 5 μm. (b) Output IDT is misrepresented in a coarsely meshed model with an element size of 10 μm.

Table 4.1. Material properties. Material properties used for the corrugated diaphragm design (HD MicroSystems 2008, Kazaryan 2000, Gad–el–Hak 2002, MEMS and Nanotechnology Clearinghouse 2009). Different types of flexible materials are used for corrugated section, flat section and for metallisation of the microdiaphragm.

MATERIAL PROPERTIES FOR DIAPHRAGM DESIGN

Material Property	PI-2610	Si_3N_4	Al
Density (Kg/m^3)	1400	3184	2770
Poisson's Ratio	0.22	0.24	0.33
Elastic Modulus (GPa)	7.5	169	71

mechanical properties of the chosen materials are shown in Table 4.1. Corrugated microdiaphragm consists of three main sections with different materials, flat section, corrugated section and the conductive thin metal section as can be seen in Figure 4.13.

Flat Section:

Silicon Nitride (Si_3N_4) was chosen for the flat part of the diaphragm, at it provides high strength over a wide temperature range, outstanding wear resistance, and good electrical insulation, hence the fluid in the pumping chamber is isolated from the electrostatic field.

Corrugated Section:

Polymer based bio–MEMS has become more and more popular mainly because it has a very low stiffness and inherently provides adequate flexibility (reduce micro-motion strain) for most of the low powered operations (Tsai and Sue 2007, Rousche *et al.* 2001). Here, polyimide PI–2610 was chosen for the corrugated section of the diaphragm. The rigid rod polyimide structure of cured PI–2600 products exhibits a desirable combination of film properties such as low stress, low coefficient of thermal expansion, high elastic modulus compared other polyimides, and good ductility for microelectronic applications (HD MicroSystems 2008). These attractive features help to generate low–stress high–displacement in the diaphragm and more importantly, facilitate comparatively easy and consistent fabrication of the corrugations around the flat section of the diaphragm.

Conductive Metal Section:

Aluminium (Al) was chosen as the material to define metal connections in the micropump device. This was mainly due to the comparatively low elastic modulus and Poisson's ratio, and low cost. However, Gold (Au) could be used as a better alternative to Al, considering the good conductivity, high biocompatibility, and the possibility in clean and neat deposition of nanometer thin layers.

4.5.5 Boundary Conditions

Once the geometry is meshed, the model needs to be then constrained by applying appropriate boundary conditions. There are two types of boundary conditions related to this model, *(i)* structural (mechanical constrains) and *(ii)* electric (electrostatic constrains) boundary conditions.

Structural Boundary Conditions:

Microdiaphragm is fully clamped to the micropump chamber and represented by constraining all the displacements of nodes associated to the wall. Since the quarter symmetry is implemented in the design to save design and simulation time, the structural symmetry condition is applied at the inner areas of the diaphragm and the air–gap as shown in Figure 4.13.

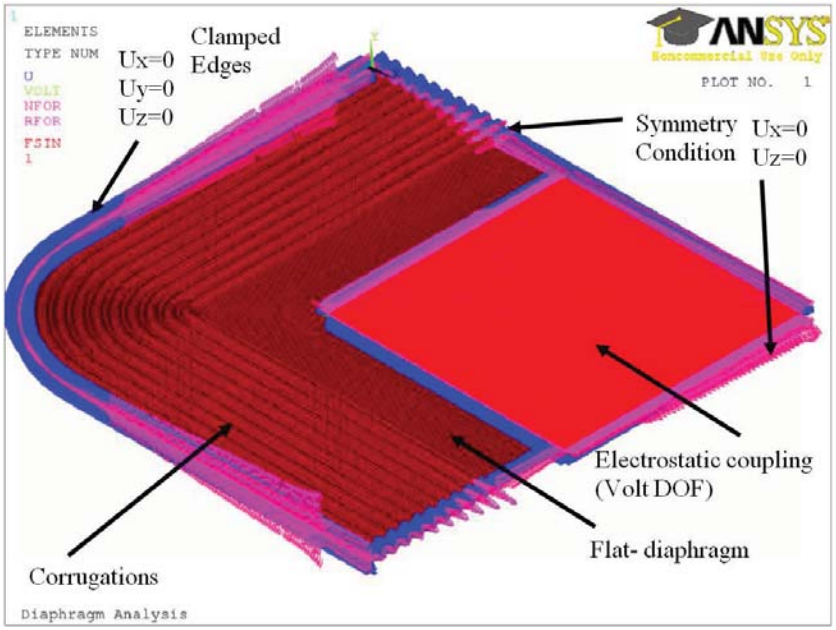

Figure 4.13. Boundary conditions applied on the design. Quarter-symmetry is exploited to reduce the simulation time and CPU usage. The dimensions of the quarter-diaphragm segment are 1000 μm $\times$ 5 μm $\times$ 1000 μm (Length/2 $\times$ Height $\times$ Width/2). Height of the air-gap is 5 μm.

Electric Boundary Conditions:

To mimic the effect of the thin conductive (Aluminium) coating at the bottom surface of the diaphragm, all the nodes on the bottom surface are coupled and a Volt DoF was applied. Additionally, to mimic the effect of the output IDT, two different sets of nodes are carefully selected at the bottom surface of the air–gap for each IDT electrode (positive and negative electrodes). As this approach negates the need for extra volumes of thin metal coating and output IDT electrodes, FEA becomes easier and more time efficient.

4.6 Simulations and Results Analysis

Results obtained from the ANSYS based FEA of corrugated microdiaphragm actuation are presented and analysed in this section. Additionally, analytical model based preliminary results are used to validate the FEA simulations.

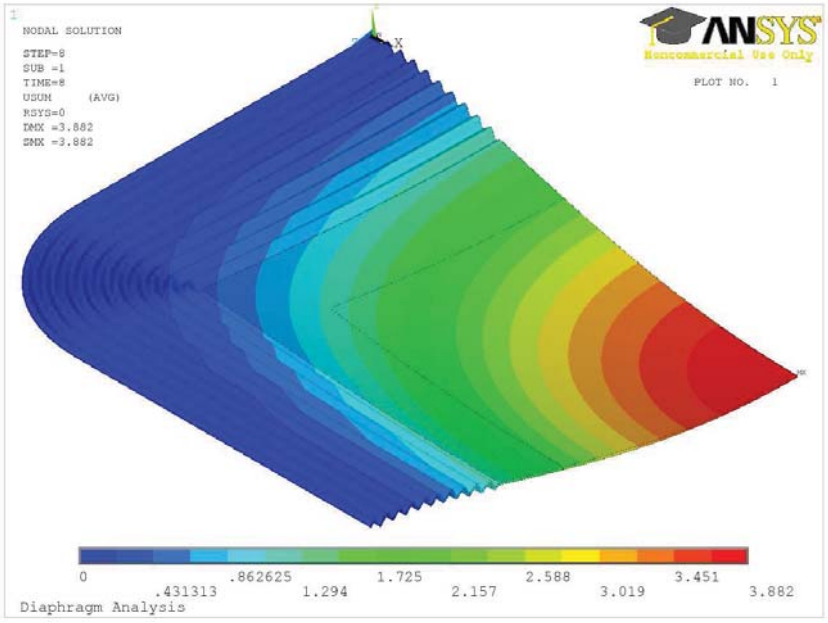

Figure 4.14. Contour plot of the displaced diaphragm. Contour plot of the displaced diaphragm structure with sinusoidal corrugations. Displacement is maximum at the middle part of the diaphragm.

4.6.1 Displacement Results for Different Types of Corrugations

As was discussed in Section 4.3, two types of sinusoidal and toroidal corrugations were designed and analysed. In these analyses, corrugation parameters (L, H, t_D and N), element types, material properties and all the other design parameters and constrains kept unchanged except the corrugation type. Therefore the mid–diaphragm displacements reflect the effectiveness of each corrugation type in the SAW device based micro-diaphragm actuation. Figure 4.14 depicts a contour plot of the simulated diaphragm structure with sinusoidal corrugations.

Deformation results acheived from FEA and analytical model for various corrugation types are presented in Figure 4.15. As expected, quadratic–shaped curves are observed, in line with the theoretical relationship between the applied electric potential and displacement. More importantly, these corrugated diaphragms have achieved higher micro–displacements for lower operating voltages, compared to flat diaphragms. The displacements achieved by any kind of corrugated diaphragm are found to be higher than that of a flat diaphragm.

It can be noted that analytical and FEA results show a good correlation in general. The apparent slight deviation in analytical results compared to FEA results is believed to

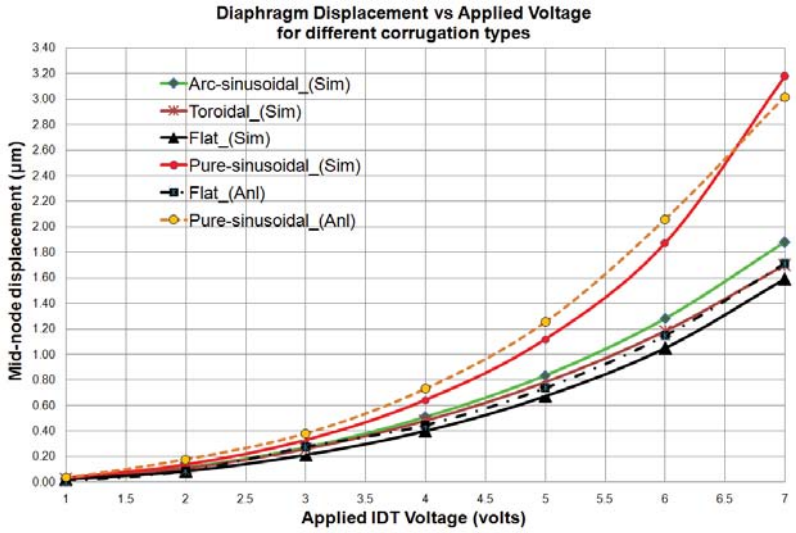

Figure 4.15. Diaphragm displacements and corrugation types. Comparison of diaphragm displacement of different types of corrugations: Pure Sinusoidal, Toroidal, Approximated sinusoidal with tangent arcs, and Flat diaphragm. Note that the corrugation parameters are L=30 μm, H=20 μm, t_D=5 μm and N=5.

be due to the simplifications made to the model during the analytical analysis. For instance, the fringe capacitance between the electrodes and IDT fingers reduces the available energy for actuation. This could cause a slight reduction in deflection achieved in the FEA model. However, such effects are not included in the analytical model, hence slightly higher deflections are observed.

Having developed the confidence in FEA, the rest of the analysis is carried out based on pure–sinusoidal type corrugations, since it has shown better deformations than other types.

4.6.2 Effect of Corrugation Wavelength

Deflections achieved by a diaphragm with pure-sinusoidal corrugations are analysed for different corrugation wavelengths (L), while keeping other corrugation parameters unchanged (H=20 μm, t_D=5 μm and N=5). FEA is carried out for different actuation voltages and the results are presented in Figure 4.16.

Higher displacements can be observed around L=15 μm and 5 μm, and the deflections tend to decrease as the corrugation wavelength increases. This is because within the selected ratio H/t_D, larger corrugation lengths increase the effective thickness of the

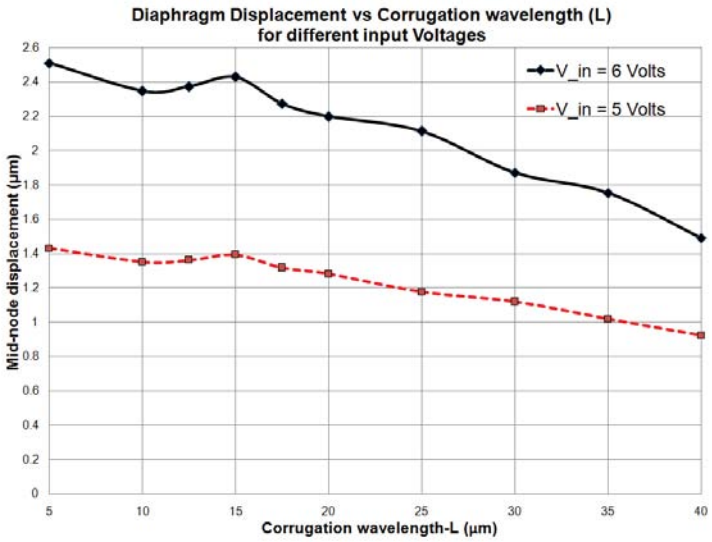

Figure 4.16. Diaphragm displacements for various L. The variation in displacement for different L, for the input IDT voltages of 5 V and 6 V, H=20 μm, t_D=5 μm and N=5.

diaphragm, hence the flexural rigidity is increased, and the mechanical sensitivity is reduced as a result (Ke *et al.* 2009). Wavelengths less than 10 μm can be discarded, because they are difficult to be fabricated.

4.6.3 Stress Distribution Around the Corrugations

Stress analysis was also carried out in ANSYS to analyse the ability of the microdiaphragm to withstand the applied mechanical forces. Contour plots of the Von Mises stress distribution around the diaphragm's corrugations for N = 5 and 10 are shown in Figure 4.17. As discussed in Chapter 3, Von Mises stress can be used to predict the yielding of any of the three materials used, under any loading condition. In either of these scenarios, the maximum Von Mises stress is less than 0.5 MPa, which is much lower than the yield strengths of the selected materials. This demonstrates that the diaphragm's deflection is well within the elastic range of the materials used. Additionally in both the scenarios, much of the stress is concentrated to the first few corrugations, and the maximum Von Mises stress values did not differ by much. Therefore, based on these simulations, it is evident that having extra corrugations does not greatly facilitate better stress distribution, but on the contrary, such an increase will result in fabrication difficulties by requiring to fabricate more corrugations.

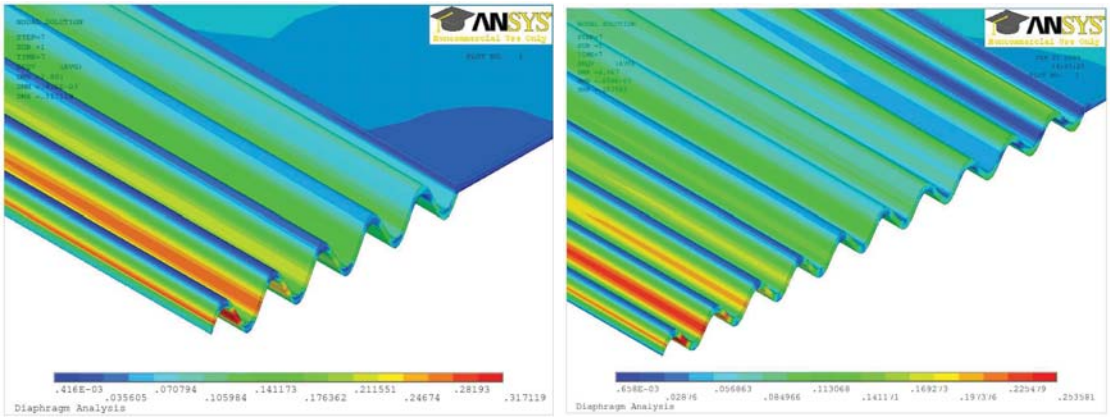

(a) Number of corrugations $N = 5$ (b) Number of corrugations $N = 10$

Figure 4.17. Von Mises Stress distribution. No great difference in Von Mises Stress is obsereved between (a) and (b) for a pure–sinusoidal corrugated design.

4.7 Fabrication and Testing of Microdiaphragms

Due to the limited availability of fabrication facilities, a preliminary microdiaphragm based actuator model was developed for initial testing, using a flat diaphragm. A pre fabricated, thin square shaped microdiaphragm (membrane) was purchased, which consisted of dimensions 2500 μm $\times$ 2500 μm $\times$ 100 nm (Length $\times$ Width $\times$ Thickness). As depicted in Figure 4.18, the membrane consists of low stress Silicon Nitride (Si_3N_4) and a supporting frame, which is made of Silicon (Si). The frame dimensions are 7500 μm $\times$ 7500 μm $\times$ 250 μm (Length $\times$ Width $\times$ Thickness).

It should be noted that the membrane structure with the supporting frame was pre made and has been prepared using a combination of several commonly used fabrication techniques. Firstly, the surface of the Silicon wafer can be uniformly covered by a support membrane of Silicon Nitride. After any thermal processing of the sample, the silicon wafer can be etched away from a small region to form the cavity. During this process Silicon Nitride layer can be used as an etch stop to facilitate easy and rapid preparation of the device (Yao *et al.* 2006). Alternatively, back–etch method can be used for membrane preparation as reported by various authors (Cole and Flemish 1992, Jin *et al.* 1998).

Once the initial preparation is carried out, the second stage etching can be used to further etch away the silicon in the small cavity, providing significant area devoid of

silicon while the Silicon Nitride membrane remains intact. For this purpose, an etchant with the highest possible etching selectivity of Silicon to Silicon Nitride is desired. As such KOH and NaOH are commonly used for this purpose (Jin *et al.* 1998, Jin *et al.* 1999). Once the Silicon is etched away, the membrane structure can be cleaned with a solvent such as acetone ($OC(CH_3)_2$) or methanol (CH_3OH).

Figure 4.18. SEM images of the microdiaphragm. The microdiaphragm structure that was used for preliminary testing of the actuation. Microdiaphragm is made of low stress Silicon Nitride (Si_3N_4) membrane and a Silicon (Si) window as a supporting structure. Thin membrane dimensions are 2500 μm $\times$ 2500 μm $\times$ 100 nm (Length $\times$ Width $\times$ Thickness). Frame thickness is 250 μm. Microdiaphragms were pre fabricated, and were purchased from Structure Probe Inc. (Structure Probe Inc. 2009).

Next, after obtaining Silicon Nitride membranes, a thin layer of gold (Au) is coated on the flat side of the membrane–window structure, using a conventional gold sputtering technique. This gold layer defines the conductive nature of the diaphragm for electrostatic actuation. During preliminary fabrication process, a simple Printed Circuit Board (PCB) is designed as the supporting electrode structure for the diaphragm. Figure 4.19 depicts this PCB, which consists of two copper (Cu) electrodes to connect the controlling signal.

Then a simple fabrication method was used to mount the gold coated diaphragm on top of the PCB electrodes. As can be seen from Figure 4.19, by utilising a simple mask made of masking tape, 5 μm thick "U" shaped gold layer is deposited on top of the outer electrode. Consequently the microdiaphragm structure is mounted on top of the gold deposition, as the final stage of the initial fabrication. For the second stage of the fabrication, the assistance and access to the facilities were obtained from Micro-Engineering Services branch at Defence Science and Technology Organisation (DSTO),

at Edinburgh, South Australia, as well as Adelaide Microscopy at The University of Adelaide.

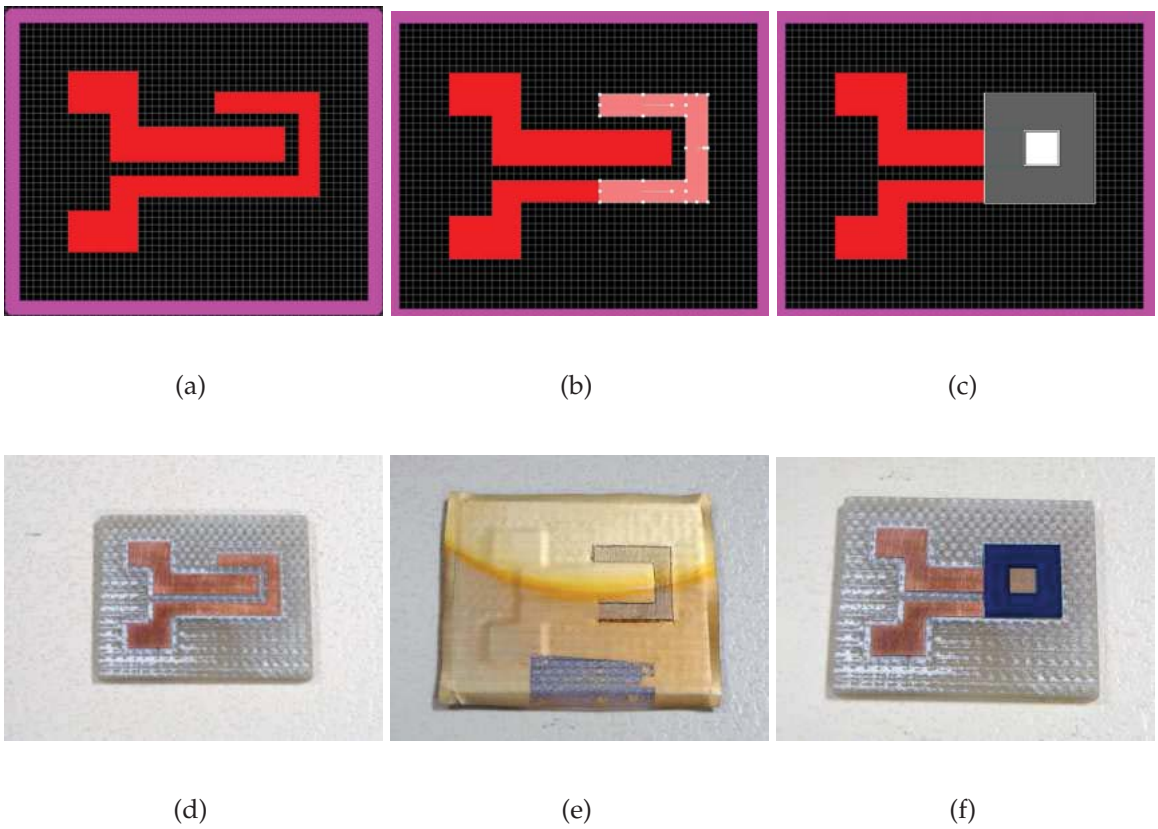

Figure 4.19. PCB design for the initial testing of microdiaphragms. (a) PCB consisting of two copper electrodes, is designed in Altium Designer. (b) The "U" shaped section in the outer electrode is designed to create the spacing between bottom electrodes and the microdiaphragm. (c) The microdiaphragm is designed to be mount on top of the "U" shaped section. (d) Manufactured PCB, consisting of copper electrodes. (e) A simple mask was used to carry out the gold sputtering to generate the required spacing. (f) The microdiaphragm is placed on top of the mid electrode with a spacing of 5 μm.

It should be noted that the fabricated device structure demonstrated only a limited level of performance and did not represent a full model of the simulated microdiaphragm structure. A better representation of the model could not be achieved mainly due to the limitations in accessing a suitable fabrication facility. Therefore the fabricated standard device is used to prove the concept of low–powered microdiaphragm actuation utilising a comparatively small actuation voltage.

Preliminary testing of the device is carried out using a PSV–400–3D Scanning Vibrometer. AC Sinusoidal input voltage with low amplitudes between 1–5 V and frequencies less than 10 Hz were used to perform this testing. As a result mid–diaphragm displacements up to 350 nm were observed. This behavior is not directly comparable with the simulated microdiaphragm with corrugations, as the tested diaphragm specifications are different to the simulated model. However, a simplified simulation was performed, incorporating the tested diaphragm dimensions onto FEM. It was observed that simulated mid–diaphragm displacements went up to 525 nm. This results mismatch between simulations and experiments were mainly due to the instability and the fragile nature in the fabricated structure. However, the potential of the proposed method can be proven from such a simple fabrication. With the availability of full access to required facilities, more comparable model can be developed and tested in future.

4.8 Discussion and Future Work

4.8.1 Issues in Microfluidic Interaction

Highly sensitive capacitive diaphragms would be suitable for sensing applications, but could cause problems in actuation applications. However, it is been shown that comparatively stiff materials in the flat section increase the overall stability of the diaphragm in similar applications (Lee and Kim 2006). Therefore the simulated design is considered to be effective and viable.

Back pressure issue is also need to be considered, which is known to affect the flow rate in valveless diffuser micropumps. This can be minimised by incorporating curved inlets in diffusers, and carefully selecting diffuser parameters such as diffuser angle and length for laminar flow condition with low Reynolds numbers (< 400) (Olsson *et al.* 2000, Olsson 1998). Following such approaches, a maximum ratio of 2.23 between forward and backward flow has been calculated for this type of diffusers, which is sufficient for a pumping effect (Woias 2001).

In micropumps, the resonance frequency of the microdiaphragm is damped by the fluidic environment around it, and various approaches have been investigated and presented in literature with successfully realised devices (Olsson *et al.* 2000, Nisar *et al.* 2008b, Lee and Kim 2006, Woias 2001). But in SAW device based interrogation, the device actuating frequency can be easily controlled without affecting the SAW frequency

and the implanted code. Therefore, an optimal operating condition can be achieved by carefully selecting a suitable control signal frequency to the device allowing sufficient relaxation and minimum energy loss (Jones *et al.* 2008, Woias 2001). These important issues are carefully addressed in Chapters 5 and 6 during the microfluidic analysis of the micropump.

4.9 Chapter Summary

In this chapter, characteristics of a corrugated microdiaphragm design was presented and the electrostatic actuation of such a diaphragm through the use of SAW device was also presented. As an extended analysis from Chapter 3, the Rayleigh–Ritz method based analytical model was developed mainly to validate the results obtained through FEA. The significance of FEA to simulate and analyse complex scenarios, as an alternative option to analytical modelling was highlighted. Moreover, FEM was carried out to evaluate the performance of corrugated microdiaphragms, and the relationship between different corrugation types, corrugation parameters, material properties, and design practices on the diaphragm performance was also presented.

It was demonstrated that the use of polyimide based sinusoidal corrugations and a square–shaped diaphragm produces more deflections compared to a flat diaphragm. Moreover, the stress distribution around corrugations were discussed. Expected future work including an overall parameter optimisation, and modelling of more complicated behavior of the micropump operation with liquid loading was also highlighted.

Additionally, a basic device structure was fabricated and tested using limited facilities. As potential future work, it was highlighted that, with the availability of better and accesible fabrication facilities, the device could be fabricated for a closer representation of the simulated structure. In Chapter 5, extensive modelling and analysis of micro diffuser/nozzle elements are presented, in view of analysing their flow rectification capability for diaphragm based micropumps.